*energies*

MDPI

*Article*

# A Finite-Element-Based Investigation of the Influence of the Production Environment on Fuel Cell Membrane Electrode Assemblies During Manufacturing

**Ling Ma *, Zhuoqi Yan, Sebastian Schabel and Jürgen Fleischer**

wbk Institute of Production Science, Karlsruhe Institute of Technology (KIT), Kaiserstraße 12, 76131 Karlsruhe, Germany

* Correspondence: ling.ma@kit.edu; Tel.: +49-173-421-6331

**Abstract:** The manufacturing process for membrane electrode assemblies (MEAs), from coating to stack assembly, is typically performed under climate-controlled conditions due to the hygroscopic properties of catalyst-coated membranes (CCMs). Large climate-controlled areas in the assembly line not only increase the energy consumption but also limit the scalability of the production line. In this study, experiments were conducted to analyze the effects of ambient humidity on the mechanical properties of a CCM. The hygroscopic swelling behavior of a commercial CCM with an ePTFE-reinforced membrane was also characterized. Using the finite element method, a 3D numerical model covering the entire MEA assembly process was developed, allowing for a numerical investigation of different climate control strategies. The influence of ambient humidity on the dimensional changes in the CCM, which leads to significant stress on the CCM due to mechanical constraints and thus to deformation of the MEA product, was simulated and validated experimentally using optical measurements. Finally, the critical steps during MEA assembly were identified, and a recommendation for the optimal humidity range for climate control was derived.

**Keywords:** MEA production; roll-to-roll; micro-environment; swelling and shrinkage behavior



**Citation:** Ma, L.; Yan, Z.; Schabel, S.; Fleischer, J. A Finite-Element-Based Investigation of the Influence of the Production Environment on Fuel Cell Membrane Electrode Assemblies During Manufacturing. *Energies* **2024**, *17*, 5737. https://doi.org/10.3390/en17225737

Academic Editors: Marcello Romagnoli and Paolo E. Santangelo

Received: 24 October 2024
Revised: 8 November 2024
Accepted: 14 November 2024
Published: 16 November 2024



## 1. Introduction

In recent years, proton exchange membrane fuel cells (PEMFCs) have been considered as a potential alternative to fossil fuels, particularly in the fields of transportation and power generation [1,2]. Although battery-electric vehicles (BEVs) have reached market readiness as passenger cars over the past few years, PEMFCs still offer significant advantages in terms of their higher gravimetric energy density and faster charging rates, making them a high-potential solution for decarbonizing long-distance heavy-duty trucks [3]. The proton exchange membrane (PEM) serves as the core component of a PEMFC, with functions including separation of the reactant gases and the conduction of hydrogen ions [4]. Catalyst layers consisting of platinum are applied to the membrane to form the so-called catalyst-coated membrane (CCM), where the electrochemical reactions take place. Alternatively, the catalyst layer can also be directly deposited onto the Gas Diffusion Layer (GDL), which is normally referred to as the Gas Diffusion Electrode [5]. Research has shown that a fuel cell prepared with a CCM exhibits a better cell performance than that of a GDE-based fuel cell because the CCM method involves higher utilization of the catalyst and a lower contact resistance in comparison to the GDE method [6]. The industrial standard has also evolved toward the CCM-based fabrication method. A CCM, two subgaskets, and two GDLs together form the membrane electrode assembly (MEA). The CCM is fixed within the subgasket frame through lamination. The subgaskets, with central cut-outs for the active area, provide mechanical support to the CCM. Furthermore, this frame-shaped edge protection helps the fragile membrane to withstand the compression force during the stack fixation process better and ensures precise positioning [1]. The GDLs on the anode and

cathode sides are then bonded to the subgasketed CCM. Because the membrane thickness is typically in the range of tens of microns, the entire handling process is particularly challenging.

Perfluorosulfonic acid (PFSA) membranes have good thermal, mechanical, and chemical stability, along with high proton conductivity, making them one of the most used membrane materials today. Since water transport plays a crucial role in the proton conductivity within PFSA membranes, they exhibit significant hydrophilic and water-absorbing properties [7]. This type of membrane was first developed and commercialized by DuPont under the trade name Nafion®. Extensive research has been conducted on the mechanical properties and moisture absorption characteristics of Nafion®. Kundu et al. measured the mechanical properties of Nafion® 112 and Nafion® 117 [8]. Tang et al. conducted tensile tests on Nafion® 112 under 16 different combinations of temperature and humidity [9]. The results revealed the fundamental relationships of the Young's modulus, proportional limit stress, and fracture stress with temperature and humidity. They also found that Nafion® 112 exhibits slight anisotropy between the machine direction (MD) and the transverse direction (TD). To develop thinner membranes with a higher strength and lower proton resistance, reinforced composite membranes were introduced by adding support materials to PFSA membranes. Expanded polytetrafluoroethylene (ePTFE) is the most well-known and extensively studied microporous material for reinforcing fuel cell membranes, both PFSA and non-PFSA membranes [10]. Due to the addition of support materials, the in-plane anisotropy of reinforced membranes is typically suppressed [7]. For example, Kolde et al. reported that fuel cells using ePTFE-reinforced membranes have a longer lifespan compared to those that use pristine PFSA membranes [11]. They also suggested that the in-plane dimensional stability of the membrane is also enhanced, which is an essential factor for the durability of fuel cells. Tang et al. tested the mechanical properties of an ePTFE-reinforced membrane under different combinations of humidity and temperature [12]. Using finite element method (FEM) simulations, they compared the in-plane stress and swelling strains of unreinforced PFSA membranes and ePTFE membranes under hygrothermal cycling in fuel cells. The results indicated that the reinforced membranes showed better durability compared to the unreinforced PFSA membranes. Coating catalyst layers onto both sides of the reinforced membranes forms catalyst-coated membranes (CCMs). Since the catalyst layers contain the same ionomers as those in the membrane, they couple with the membrane components and may affect the mechanical properties of the membrane [1]. For example, Goulet et al. found that the swelling strain of the CCM at the same humidity level is half that of pure PFSA membranes, and they observed that the catalyst improves the mechanical properties of the membrane [13]. Uchiyama et al. compared the mechanical properties of NR211 membranes and catalyst-coated NR211-CL membranes, similarly finding that NR211-CL exhibits a higher mechanical strength and a lower swelling strain compared to NR211 membranes [14]. Various studies have investigated how the swelling and shrinkage behavior of PFSA membranes accelerates mechanical degradation due to wet–dry cycles during fuel cell operation [15,16]. However, the dimensional instability of the membrane due to humidity changes is equally critical during manufacturing processes, particularly in mass production scenarios. An uncontrolled production environment can lead to significant quality issues and increased scrap rates, which is a critical aspect that has received little attention in the literature and will be specifically addressed in this present work.

To meet the production yield and precision requirements in MEA manufacturing, the roll-to-roll (R2R) process has been proposed, investigated as a viable replacement for the current pick-and-place-based sheet-to-sheet assembly processes [17,18]. Typically, in the R2R process of film production, the internal stress within the flexible substrate must be controlled precisely to ensure product quality and productivity [19]. Humidity deviations will cause the CCM to absorb or desorb water molecules, leading to changes in its dimensions [12]. As the CCM is constrained by the subgasket at the perimeter after the lamination process, the swelling and shrinkage behavior of the membrane is a critical factor in the assembly process. However, this process can lead to various defects,

such as wrinkling and yielding of the membrane, as well as bending and bulging of the MEA [20–22]. In the past decade, numerous FEM models have been developed and reported in the literature for studying the mechanical durability of membranes under hygrothermal cycling during fuel cell operation [14,23,24]. Most of these models have focused on the out-of-plane stresses, which are induced by the fuel cell's bipolar plates. However, the in-plane stresses due to fluctuations in web tension and deformation due to humidity variations during the R2R process of MEA assembly cannot be ignored. Currently, few studies have addressed this aspect.

In this study, we investigated the mechanical properties of a commercial ePTFE-reinforced CCM under different humidity conditions using tensile tests conducted in an environmental chamber. Parameters such as the elastic modulus and proportional limit stress were examined, and the moisture absorption and desorption behavior were measured under specific humidity conditions. The elastic properties of the GDL and the subgasket were ascertained at room temperature. A numerical model using the finite element method was developed to cover the local climate control during different MEA manufacturing processes. The focus was on simulating the effect of humidity on dimensional changes in the CCM, which can lead to deformation of MEA products.

## 2. Materials and Methods

The CCM used in this study was a GORE® PRIMEA® CCM (W. L. Gore & Associates GmbH, Putzbrunn, Germany) based on the Gore-Select® 8 µm membrane and had a Pt loading of 0.4 mg/cm$^2$ on the cathode side and 0.1 mg/cm$^2$ on the anode side. The thickness of the CCM itself was measured as 0.03 mm. According to the DIN EN ISO 527-3 standard [25], it was cut into strip specimens with a width of 20 mm and a length of 150 mm. Tensile tests were conducted using the Zwick Roell material testing system zwickiLine (ZwickRoell GmbH & Co. KG, Ulm, Germany), with the temperature and humidity controlled in the environmental chamber. The test setup is shown in Figure 1. The experimental temperature was set to 21 °C since the R2R assembly process for a CCM usually occurs at room temperature [26]. The hygroscopic expansion coefficient and stress–strain curves of the CCM were measured at five different humidity levels (25%, 40%, 50%, 60%, and 75%). This humidity range encompassed the typical laboratory conditions, with 21 °C and 50% representing the industry standard for MEA manufacturing. Additional humidity levels were selected to enable precise interpolation of the swelling expansion coefficient.

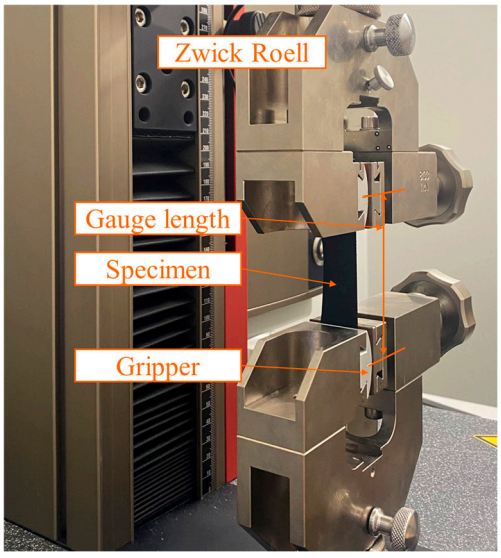


**Figure 1.** Membrane tensile test setup.

Before starting the experiment, the gauge length of a pair of wedge grips was set to 75 mm. Once the specimen was clamped into place, a preload of 0.001 N–0.002 N was applied to ensure it remained straight throughout the test and to eliminate the slack caused by hygroscopic expansion. Stabilizing the initial temperature and humidity in the environmental chamber for 16 h allowed the set values to be achieved and maintained. During this process, the length of the CCM changed due to the swelling or shrinkage behavior, which was recorded using the universal testing machine. Figure 2a shows an example of the strain in the CCM plotted over time when the temperature is 21 °C and the humidity increases from 60% to 75%. The first derivative curve of this strain–time curve is shown in Figure 2b. From this figure, it can be observed that after the humidity reaches the set value and is maintained for 5400 s (1.5 h), the strain rate and the dimensional changes stabilize, indicating that the CCM reaches a saturated state. The gauge length of the specimen is now the original length plus the displacement of the grips. The recorded change in the crosshead is considered a measure of the dimensional changes due to variations in humidity. For all tests, the crosshead speed was set to 5 mm/min according to the DIN EN ISO 527-3 standard. It should be noted that the mechanical strength of the CCM also changes with the humidity variations. Therefore, the recorded crosshead displacement represents the total strain $\varepsilon^{tot}$ in the CCM due to changes in humidity, which is the sum of the elastic strain $\varepsilon^{el}$ and the humidity-induced strain $\varepsilon^{RH}$, as shown in Equation (1).

$$\varepsilon^{tot} = \varepsilon^{el} + \varepsilon^{RH} \tag{1}$$

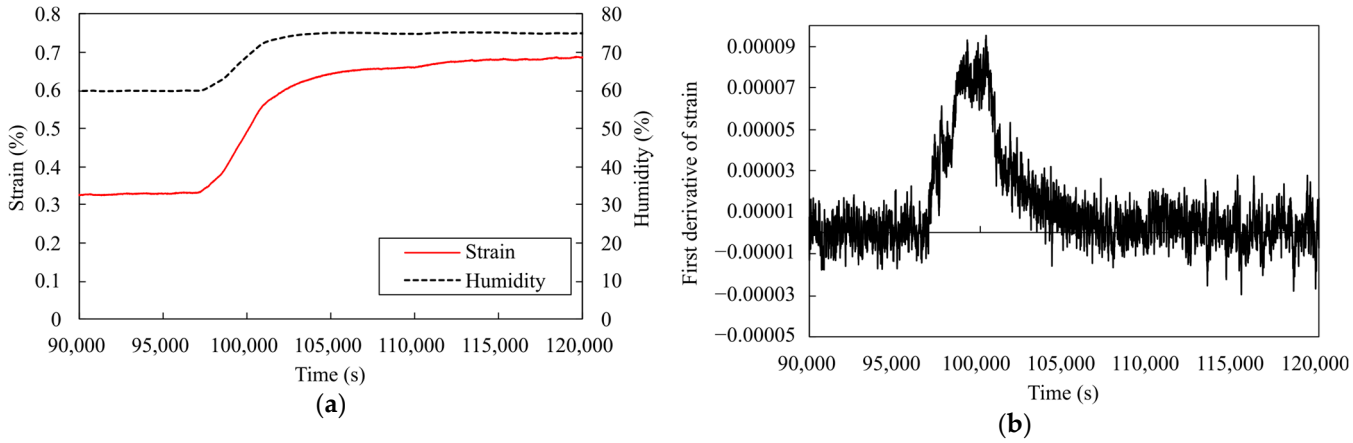


**Figure 2.** (**a**) Curves for strain and humidity with time variation during the experiment; (**b**) the curve of the first derivative of strain with time variation.

Tensile tests until failure were also conducted at each humidity level. The stress–strain relationship was calculated from the force–displacement data recorded during the tensile testing. Based on this relationship, the elastic modulus, yield strength, and hygroscopic expansion coefficient of each specimen at specific humidity levels were determined. The mechanical properties of the GDL and the subgasket are not significantly affected by temperature and humidity. Commercially available subgasket and GDL materials were used for the experiments. The GDL used in this work was a non-woven felt-like fiber fleece H14CX653 from Freudenberg. And for the subgasket, a polyethylene naphthalate (PEN) film with a one-sided polyester-resin-based heat-seal adhesive layer from CMC Klebetechnik GmbH was chosen. The mechanical properties of the GDL and the subgasket at room temperature were measured using similar experimental procedures. To express the orthotropic material behavior of the GDL [27], the Young's modulus was obtained for both the in-plane and out-of-plane directions, where the subscripts x, y, and z represent the machine direction, transverse direction, and the direction through thickness, respectively. The results are shown in Table 1.

**Table 1.** Mechanical properties of the GDL and the subgasket.

| Material | Density (g/mm$^3$) | Poisson's Ratio | $E_x$ (MPa) | $E_y$ (MPa) | $E_z$ (MPa) | Yield Stress (MPa) |
|---|---|---|---|---|---|---|
| GDL | $6.25 \times 10^{-4}$ | 0.25 | 3380 | 950 | 4.5 | 8.90 |
| Subgasket | $1.30 \times 10^{-3}$ | 0.34 | 1973.00 | - | - | 110.30 |

## 3. Experimental Results

### *3.1. Mechanical Properties*

Figure 3a,b show the true stress–strain curves of the CCM in the MD (machine direction) and the TD (transverse direction) at different humidity levels. Unlike traditional metal materials, which experience a region of Hookean (linear) behavior, the CCM shows viscoelastic properties [28,29]. Therefore, referring to the ASTM D882 standard [30], the tangent modulus should be applied to describing the material's stiffness in the designated region, where the processability plays a more important role. We referred to the method by Tang et al., defining a proportional limit stress to describe the onset of the yield [9,12], as shown in Figure 4. Table 2 summarizes the Young's modulus and the proportional limit stress of the CCM at different humidity levels. The mechanical properties of the CCM exhibit anisotropy. The E modulus and the proportional limit stress of the CCM in the MD are higher than those in the TD. In the TD, these values decrease significantly with an increase in humidity. However, in the MD, this trend of variation is not evident. The Poisson's ratio of the membrane is not significantly affected by humidity, so in this study, the Poisson's ratio at 50% humidity is used as a constant value.

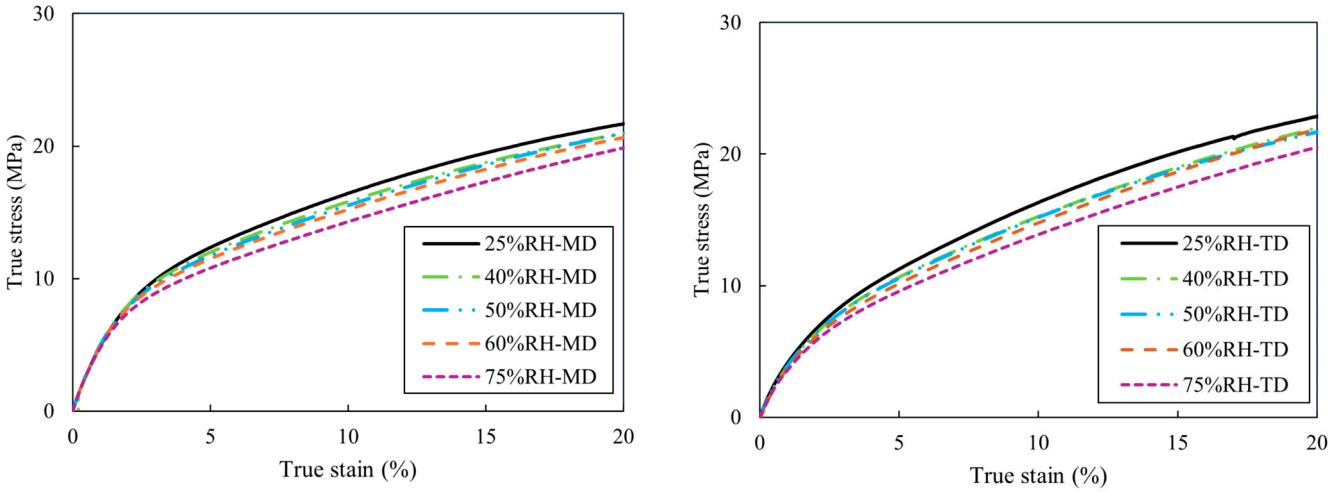


(**a**) (**b**)

**Figure 3.** Stress–strain curves for CCM at different humidity levels: (**a**) MD; (**b**) TD.

**Table 2.** Mechanical properties of CCM at different humidity levels.

| Relative Humidity (%) | Density (g/mm$^3$) | $E_{MD}$ (MPa) | $E_{TD}$ (MPa) | Poisson's Ratio | Proportional Limit Stress in MD (MPa) | Proportional Limit Stress in TD (MPa) |
|---|---|---|---|---|---|---|
| 25 | $1.5 \times 10^{-3}$ | 593.80 | 499.30 | 0.3 | 6.63 | 5.00 |
| 40 | $1.5 \times 10^{-3}$ | 587.53 | 478.41 | 0.3 | 6.08 | 4.73 |
| 50 | $1.5 \times 10^{-3}$ | 588.30 | 477.41 | 0.3 | 5.84 | 4.49 |
| 60 | $1.5 \times 10^{-3}$ | 576.42 | 453.40 | 0.3 | 5.65 | 4.24 |
| 75 | $1.5 \times 10^{-3}$ | 568.62 | 347.25 | 0.3 | 5.47 | 3.98 |

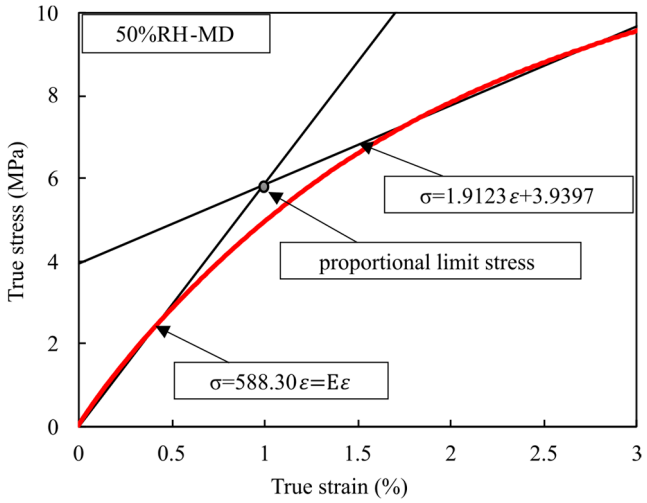


**Figure 4.** Definition of the secant modulus and the proportional limit stress (50% RH, MD).

### *3.2. Hygroscopic Expansion Properties*

Due to the hydroscopic nature of PFSA, the membrane will swell with increasing humidity and contract due to water loss. This can cause stress and deformations between the CCM, the subgasket, and the GDL during assembly. Therefore, the total strain in the MD and TD at 40%, 50%, 60%, and 75% relative humidity was measured. The hygroscopic expansion strain caused by moisture absorption was calculated as the total strain minus the elastic strain generated by 0.001 N, as shown in Figure 5. As the humidity increases, the swelling strain of the CCM increases, and the CCM's swelling is isotropic. Since Abaqus does not have a material model built in for defining the hygroscopic swelling coefficient, the relative humidity was input into the model as a predefined field. The hygroscopic expansion coefficient could then be defined as a field-dependent expansion of the material property. Referencing the field expansion coefficient formula in Abaqus, the hygroscopic expansion coefficient $\alpha_H$ is defined as shown in Formula (2), where $\alpha_h$ is the hygroscopic expansion coefficient, $\varepsilon_n$ the strain value under different humidity, $f_n$ the reference value of predefined humidity $n$ for the field expansion coefficient, and $f_0$ the initial value of predefined humidity $n$.

$$\alpha_h = \varepsilon_n / (f_n - f_0) \quad (2)$$

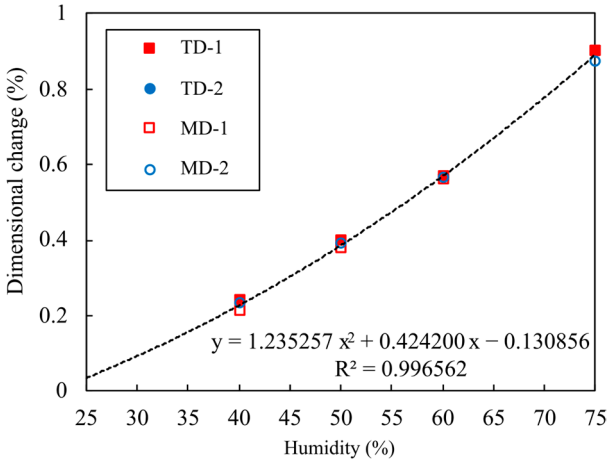


**Figure 5.** Dimensional change as a function of relative humidity at various humidities.

The quadratic fitting of the humidity expansion coefficient shows good accuracy (Figure 6). The formula for the hygroscopic expansion coefficient is obtained as follows:

$$\alpha_h = -0.000000067h^2 + 0.000011063h - 0.000235867 \quad (3)$$

where $h$ is the humidity value, and $\alpha_h$ is the humidity expansion coefficient. Based on this formula, the humidity expansion coefficient is introduced into Abaqus at each 1% humidity interval.

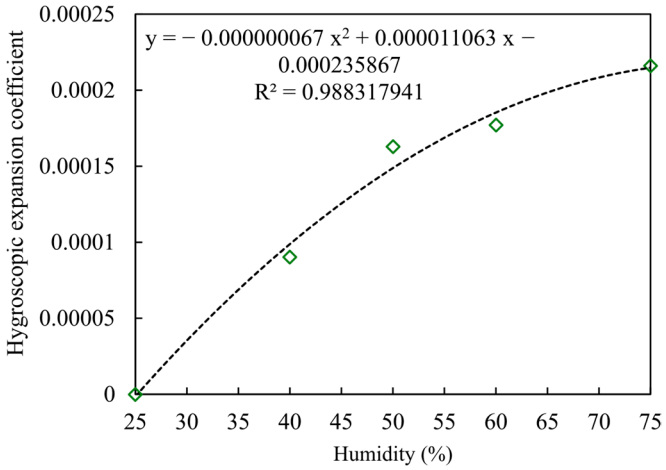


**Figure 6.** Hygroscopic expansion coefficient at different humidity levels and the fitted curve.

## 4. FEM Analysis of the MEA Production Process

### *4.1. The Model and Assumption*

The model simulating the MEA manufacturing process was constructed as a five-layer structure, including two subgaskets, a CCM with full-area catalyst coatings on both sides, and two GDLs on the anode and cathode sides, which is a widespread industrial design among fuel cell manufacturers [31–34]. A schematic illustration and a cross-section of the five-layer MEA used in this research are shown in Figure 7. It is worth mentioning that while the GDL does not initially make contact with the CCM during the assembly process in this MEA configuration, contact will be established during the stacking process through compression forces. Since the thicknesses of all the components are significantly smaller than the in-plane dimensions, the 3D shell element was selected for all components. The geometric parameters are shown in Table 3. The subgaskets were only modeled with the window as the active area, and the manifold areas for the gas inlets and outlets were neglected for simplification.

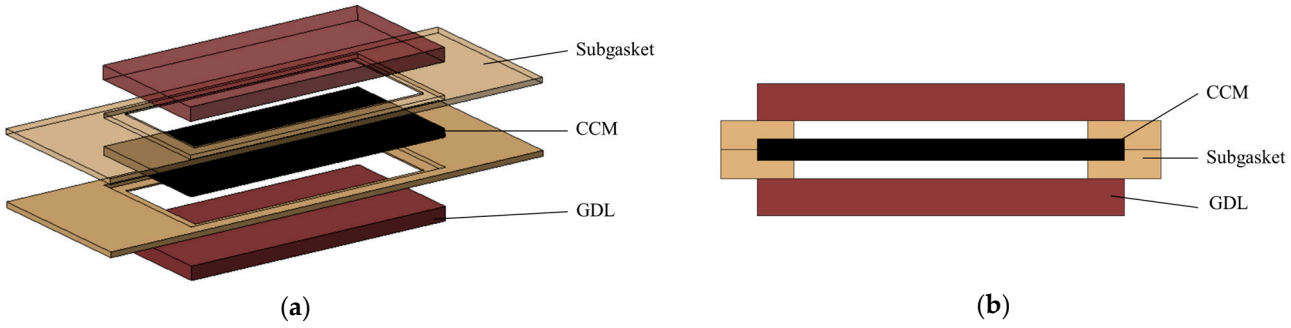


**Figure 7.** Schematic views of the MEA design (**a**) 3D illustration; (**b**) cross-section (not true to scale).

**Table 3.** Geometric parameters of the MEA components.

| | Length (mm) | Width (mm) | Thickness (mm) |
|---|---|---|---|
| CCM | 200 | 116 | 0.030 |
| GDL | 200 | 116 | 0.185 |
| Window for active area | 194 | 110 | 0 |
| Subgasket | 360 | 136 | 0.040 |

In R2R processes, the influence of web tension cannot be ignored. Based on the experimental setup, in this FEM model, the web tension is simplified by applying a displacement boundary condition of 0.02 mm on the right side of the MEA to ensure that this four-layer structure of the MEA is under tension [35,36]. The left edge is assigned as a fixed constraint. The connections between the CCM, the subgasket, and the GDL are adhesive. Since this study did not focus on adhesive connections, a TIE connection was used to simplify the definition of the adhesive interaction between the MEA components. Due to the high density and elastic modulus of the adhesive used in the MEA assembly process, the GDL was divided into two sections: the active area section and the overlap section. Different material properties were defined for each section. The area applied with adhesive was assigned a higher density and Young's modulus. Additionally, gravity loading was added in the first step of the FEM model to make the FEM more closely resemble the actual experimental conditions. Typically, the temperature variation in a factory is estimated to be between 20 and 30 °C. The mechanical properties of the CCM do not vary significantly within this temperature range. Therefore, the simulation temperature in this study was set to room temperature (21 °C) and kept constant throughout the simulation. As described in Section 3.2, the relative humidity was introduced into the model through a predefined field, as in the humidity field in this case. By invoking the field-dependent expansion property of the CCM, the swelling-induced strain could be simulated.

In state-of-the-art production lines, subgaskets are always supported by a carrier film or a vacuum conveyor belt and are therefore not easily deformed. Hence, the FEM model simplified the adhesive process between the subgasket and the CCM. The assembly process of the MEA is simulated in four steps:

Step 1 The web tension was applied in the form of a shell edge load onto the subgaskets. The initial temperature and humidity fields were set up to 21 °C and 50% RH (RH0, ideal conditions). The temperature was held constant throughout the rest of the simulation.

Step 2 The CCM was disposed between two subgaskets with adhesive components. The humidity was changed linearly from the initial conditions to the next humidity level (RH1).

Step 3 One GDL was glued onto the bottom of the subgasketed CCM. The humidity level was again modified (RH2).

Step 4 The second GDL was attached to the other side of the subgasketed CCM to form a five-layer MEA. The humidity level was set up to the next potential value (RH3).

### *4.2. Validation of the FEM Model*

To validate this finite element model, the focus was placed on the third step of the MEA assembly process. First, an MEA with a four-layer structure, including a CCM, two subgasket layers, and a GDL at the bottom, was fabricated at 50% humidity. The experimental setup is shown in Figure 8. The MEA was first attached to a metal frame on both sides and stretched tight. Two sets of experiments were conducted, one under a hydration cycle of 50%-60%-75% and the other under a dehydration cycle of 50%-40%-25%. Each humidity level was maintained for 16 h to ensure that the CCM's deformation reached a stable and equilibrium state. The out-of-plane displacement of the CCM was recorded using an industrial 3D camera (ATOS Q, Carl Zeiss GOM Metrology GmbH).

Various reference markers (supplied by GOM) were applied onto the CCM's surface. The swelling- and shrinkage-induced geometrical irregularities like buckling and wrinkling were tracked and recorded through automatic recognition of the reference markers by the GOM system. Using the center point of the CCM as the origin, the out-of-plane displacement was measured in both the X- and Y-directions and compared with the results from the FE model. The results are shown in Figure 9. It can be seen that the experimental and simulation results agree qualitatively in capturing key behavioral trends regarding the swelling- and shrinkage-induced buckling behavior of the CCM. Furthermore, the magnitude and the location of the out-of-plane displacement could also be prognosed. The deviation in Figure 9b,d) between the finite element simulation results and the experimental results may be attributed to the non-ideal symmetric conditions in real situations, such as assembly errors and the initial wrinkles present in MEAs that are manually assembled and laminated. Therefore, it can be inferred that the boundary conditions and material parameters used in the model are reasonable.

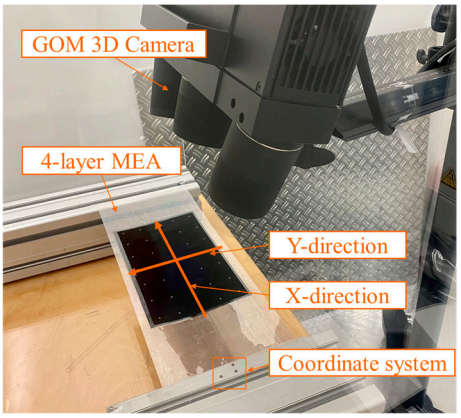


**Figure 8.** RH variation experiment for 4-layer MEA.

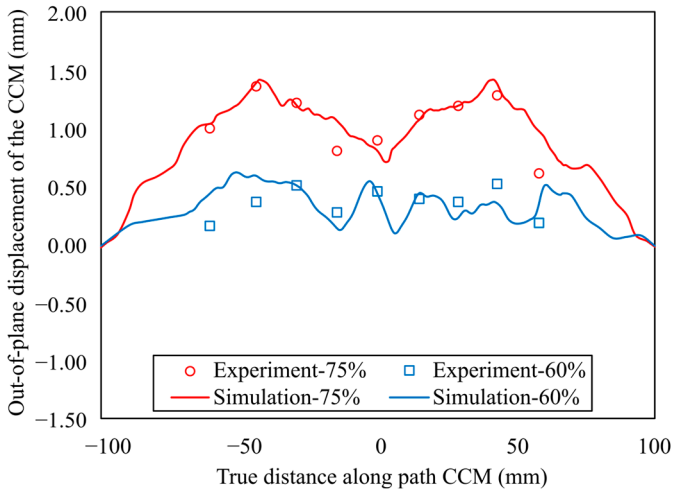


(**a**) 50%-60%-75% humidity: X-direction

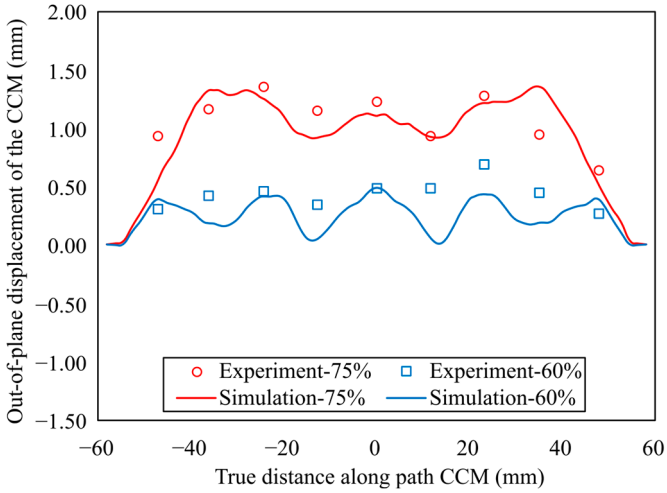


(**b**) 50%-60%-75% humidity: Y-direction

**Figure 9.** *Cont.*

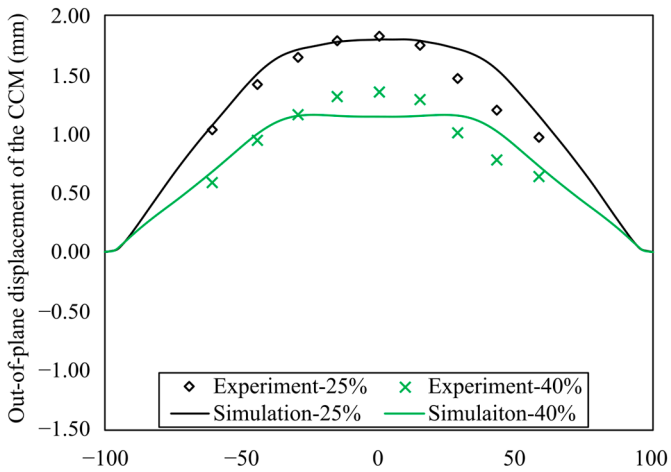


(**c**) 50%-40%-25% humidity: X-direction

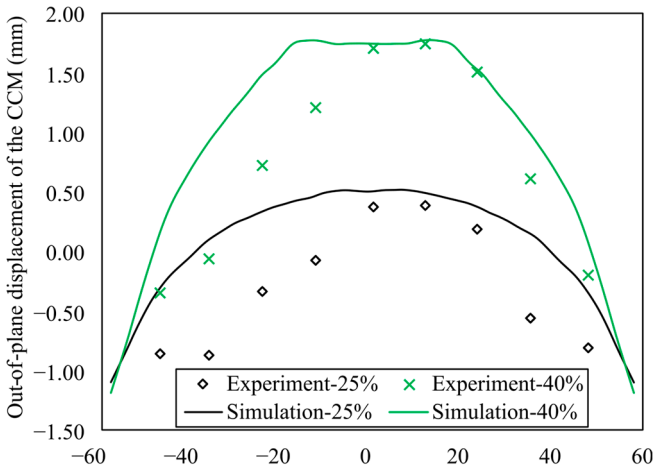


(**d**) 50%-40%-25% humidity: Y-direction

**Figure 9.** Comparison of experimental and finite element simulation results for out-of-plane displacement of the CCM. (**a**) 50%-60%-75% humidity in X-direction; (**b**) 50%-60%-75% humidity in Y-direction; (**c**) 50%-40%-25% humidity in X-direction; and (**d**) 50%-40%-25% humidity in Y-direction.

## 5. Results and Discussion

The first objective of the simulation was to ascertain the effect of humidity on the final assembled five-layer MEA. The FEM simulations were conducted with relative humidity (RH) variations between 50%-60%-75%-50% and 50%-40%-25%-50%, and the stress distribution in the CCM and the deformation of the entire MEA were compared. As shown in Figure 10a, it can be seen that the change in humidity from 50% to 75% initiates water absorption and a swelling effect in the CCM, while the edge constraints of the subgasket hinder the expansion of the CCM. Therefore, the magnitude of stress on the CCM in the region in contact with the subgasket is higher than in the central region. When the humidity is cycled back to 50%, there is a residual stress of 0.027 MPa on the CCM seen. In the dehydration process (Figure 10b), the change in humidity from 50% to 25% causes the CCM to lose water and contract. The subgasket and the GDLs have a greater thickness and a higher stiffness, which hinder the contraction of the CCM. As a result, significant stress on the CCM is shown. Consequently, when the humidity is cycled back to 50%, an average residual stress of 0.43 MPa remains on the CCM. Dehydration has a more critical impact on the MEA. It is therefore recommended that the storage environment for the MEA should not experience excessive reductions in humidity.

Since the GDLs and subgaskets are assembled symmetrically to the CCM in the five-layer MEA, only the in-plane stress variations in the upper GDL and the subgasket under different humidity cycles are presented here, as shown in Figure 11. From the figures, it can be seen that compared to the GDL, the subgasket experiences less stress due to the expansion or contraction of the CCM. The bonded area of the GDL has relatively low stress due to the higher stiffness of the dry adhesive, while the areas adjacent to the bonded region of the GDL experience higher stress. Notably, when the relative humidity decreases to 25%, stress concentrations of 8.4 MPa occur at the four corners of the GDL, which is one magnitude higher than the hydration-induced stress of the GDL and even approaches the yield strength. Therefore, at very low relative humidity, there is a risk of GDL fracture. When the relative humidity returns back to 50% after hydration or dehydration, residual stresses of 0.09 MPa and 1.59 MPa can be observed on the GDL, respectively. Residual stress caused by reductions in humidity will potentially have a negative impact on the fuel cell's lifespan after stacking.

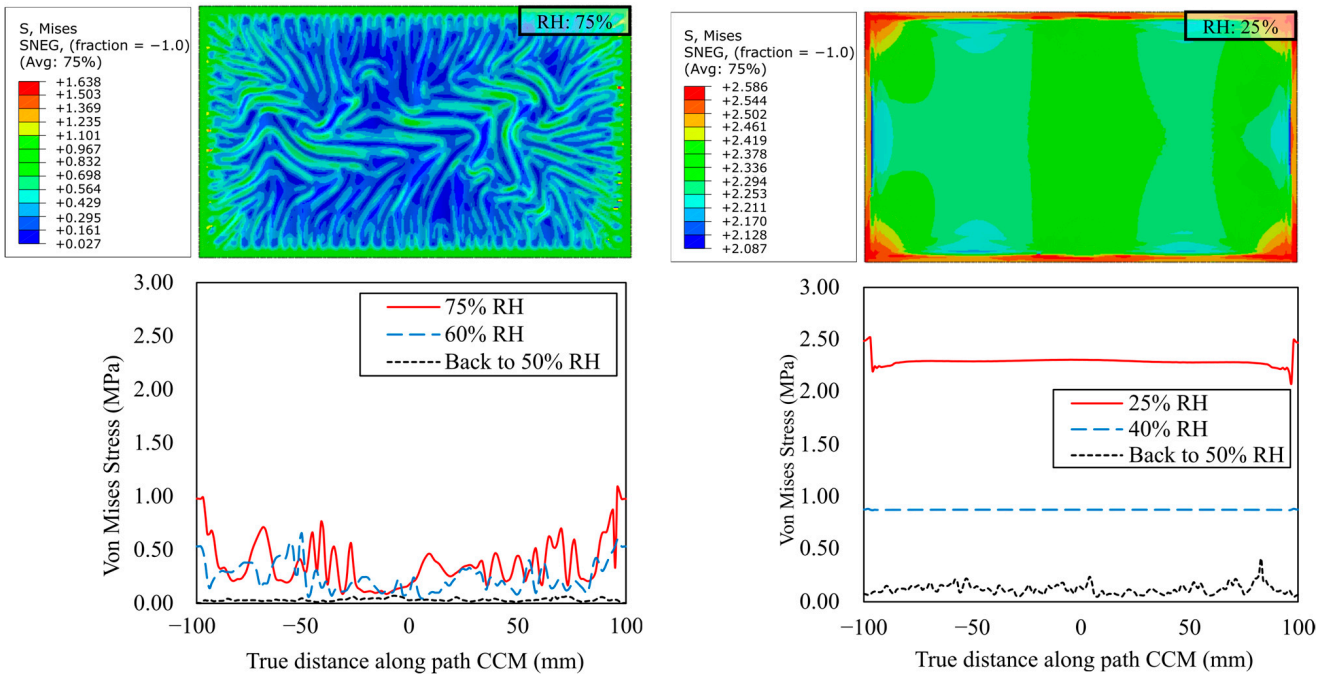


**Figure 10.** Von Mises stress states of the CCM and stress distribution along the middle path under humidity changes: (**a**) hydration cycle and (**b**) dehydration cycle.

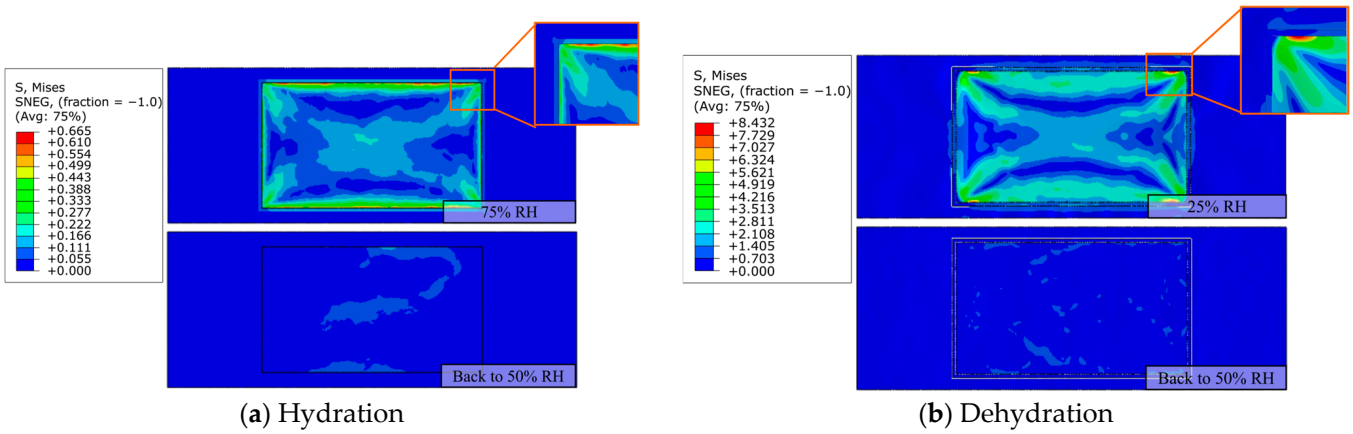


**Figure 11.** Stress variations in the upper GDL and the subgasket under different humidity cycles.

Figure 12 shows the cross-sectional shape of the MEA in the Y-direction when the MEA returns to its initial humidity after experiencing an increase or decrease in humidity. The wrinkles caused by the hygroscopic expansion of the CCM do not fully recover when the humidity returns to the initial level, and flattening the CCM may require further lowering of the humidity. The reduction in humidity causes the CCM to shrink, resulting in bending of the MEA but no wrinkling of the CCM.

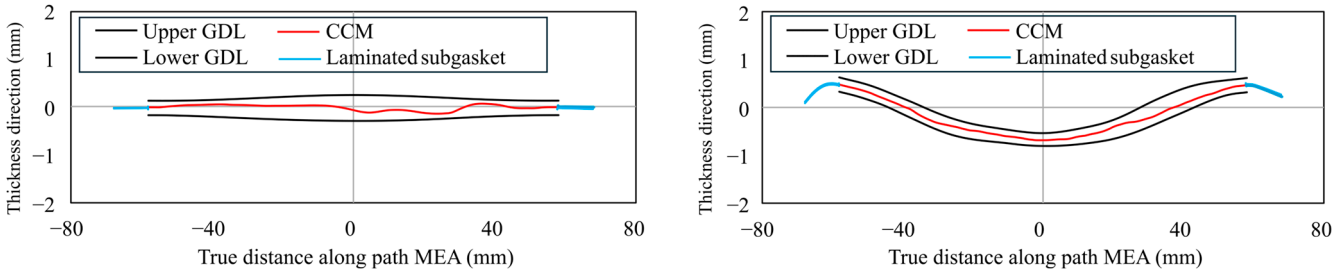


(**a**) Hydration (**b**) Dehydration

**Figure 12.** The cross-sectional shape of the MEA in the Y-direction when the MEA returns to the initial humidity.

To further investigate and identify the key step most affected by changes in humidity, eight different simulations were conducted, where the fluctuations in humidity occurred between step 2 and step 3 or step 3 and step 4. The humidity in the other steps was maintained at or cycled back to 50%. Figure 13 shows the maximum in-plane stress of the CCM at each step during the different humidity fluctuations. Due to the constraining effect of the subgasket on the CCM (in the three-layer MEA) and the compressive effect of the GDL on the wrinkled CCM (in the four-layer MEA), regardless of at which step the hydration occurs, the in-plane stress of the CCM increases, possibly due to the compression of the wrinkled CCM by the GDL. Humidity changes in the three-layer MEA structure result in a greater increase in the in-plane stress in the CCM in the next step than the increase after humidity changes in the four-layer structure. This is because the installation of the GDL stabilizes the size of the active area in the subgasket. To explain the mechanism of this phenomenon better, Figure 14 compares the deformation in the Y-direction of the MEA. The upper images in Figure 14a,b represent when the humidity change occurs at step 2 and the lower images when it occurs at step 3. From the figures, the stabilizing effect of the GDL on the size of the active area in the MEA can be observed more clearly. As the relative humidity increases, the active area of the three-layer MEA expands outward. However, the shape of the active area of the four-layer MEA does not change. When the relative humidity decreases, the inward shrinkage of the active area in the three-layer MEA's subgasket is almost twice that of the four-layer MEA. If humidity changes occur before the GDL is installed, the subsequently installed GDL will hinder the shrinking or swelling of the CCM, leading to higher in-plane stress on the CCM and possibly even causing plastic deformation. From this, it can be observed that humidity changes have the least impact when they occur on an MEA that already has one GDL assembled. Irrespective of the step at which the humidity is reduced to 25%, the stress on the CCM exceeds the maximum linear elastic range.

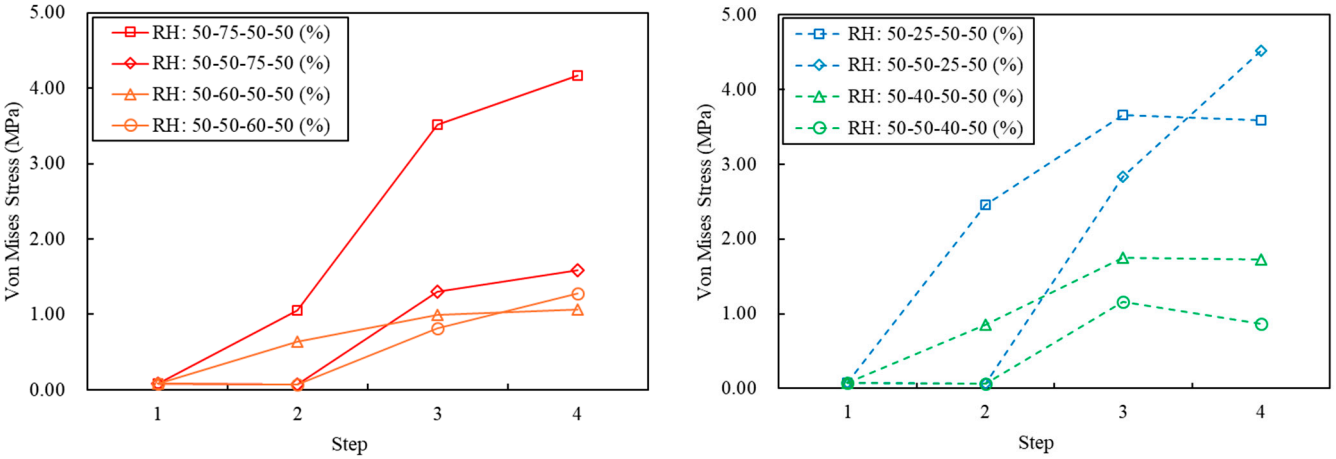


(**a**) Hydration (**b**) Dehydration

**Figure 13.** The maximum in-plane stress of the CCM at different steps: (**a**) hydration and (**b**) dehydration.

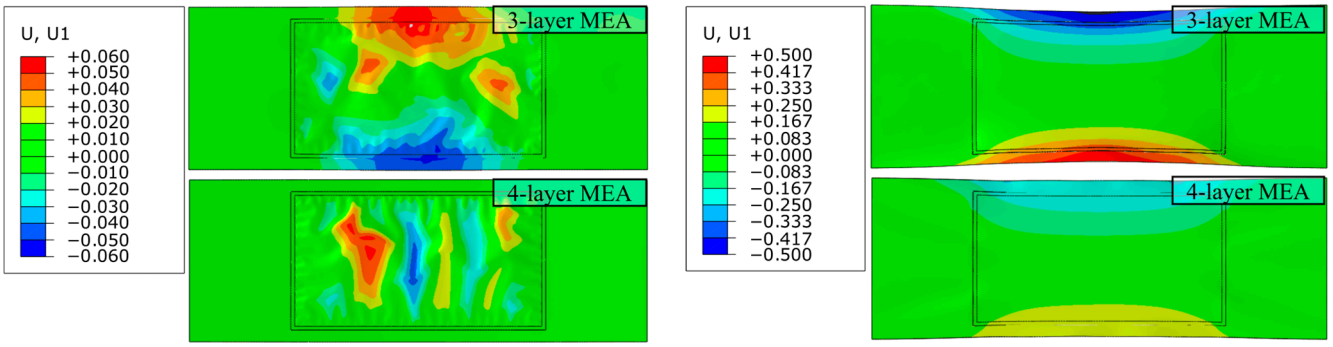


(**a**) RH: 50%-75% (**b**) RH: 50%-25%

**Figure 14.** Deformation of MEA during hydration and dehydration in Y-direction: (**a**) RH: 50%-75% and (**b**) RH: 50%-25%.

At the same time, the dimensional accuracy of the MEA plays an important role in both the electrochemical performance and operational lifespan of a PEMFC. While the impact of the minimum residual stress on the cell's performance is unclear, residual deformations in the form of wrinkles can be extremely critical, especially when considering that the final stack will be compressed at a certain force to improve the volumetric energy density and reduce the mass transport resistance. Figure 15 shows the cross-sectional shapes of the final five-layer MEA in each component. The results of all the simulations with dehydration to 25% are excluded since the maximum in-plane stress of the CCM approaches the proportional limit stress. The lower GDL is then installed at the beginning of the third step. The figure indicates that the FEM simulations with the 50-75-50-50 (%), 50-60-50-50 (%), and 50-50-40-50 (%) humidity sequences result in significant bending deformation in the lower GDL and the whole MEA. In the FEM results with humidity sequences of 50-40-50-50 (%) and 50-50-40-50 (%), the CCM exhibited severe wrinkling. A schematic is shown in Figure 16 to analyze the causes of the deformation in the MEA. The shape of the active area is stabilized by the relative higher stiffness of the GDL compared to the three thin plastic films. This means that any humidity disturbance before and after the initial installation of the first GDL is critical. The key point is not whether it is currently in the ideal state or not but how the relative humidity changes between those two states. If the relative humidity increases, the CCM will wrinkle, and conversely, the GDL will bulge. Once the first GDL is installed, an increase in humidity will not affect the size of the active area because the swelling force of the CCM cannot overcome the stiffness of the

GDL. However, the tendency of the CCM to shrink can still generate enough tension to cause the GDL to bulge, keeping the dehydration process critical at this stage.

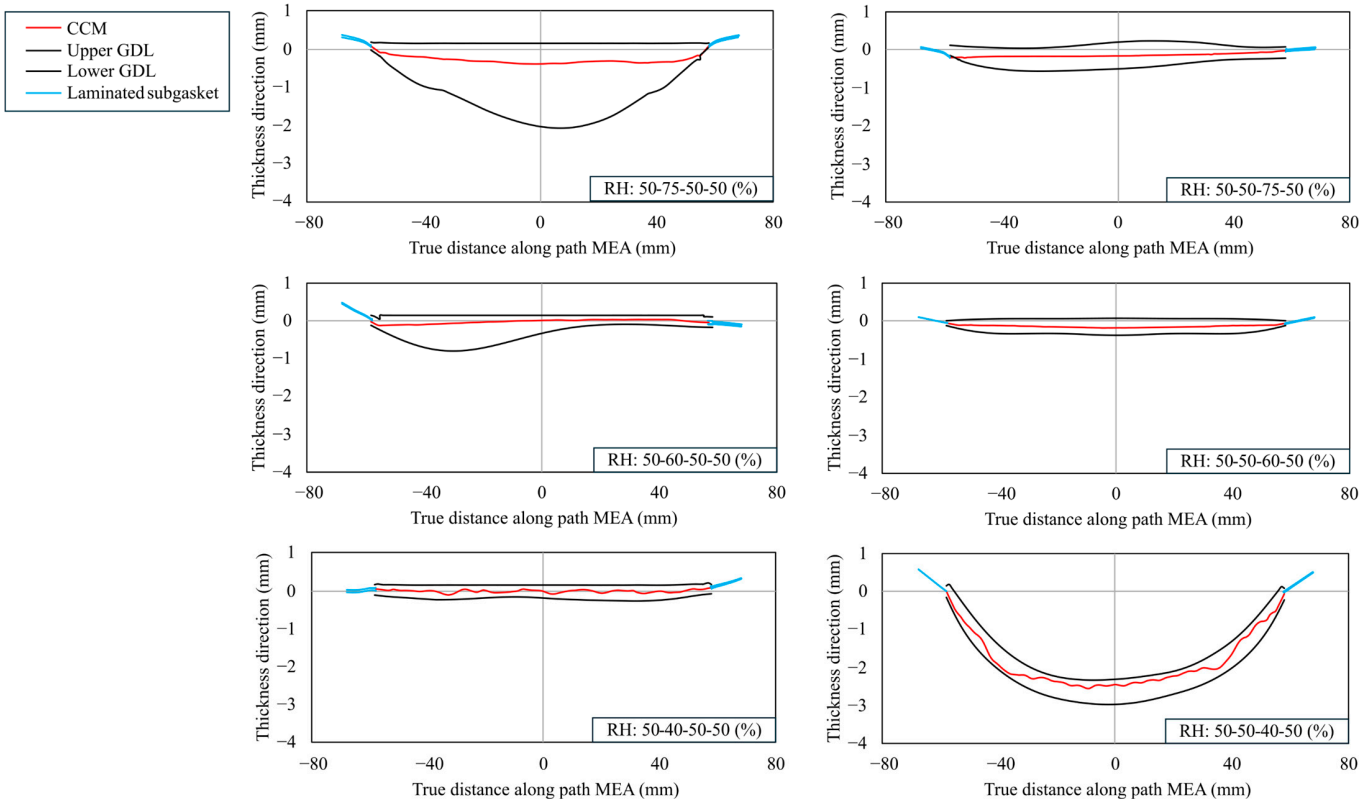


**Figure 15.** Cross-sectional shapes of five-layer MEA during different humidity changes.

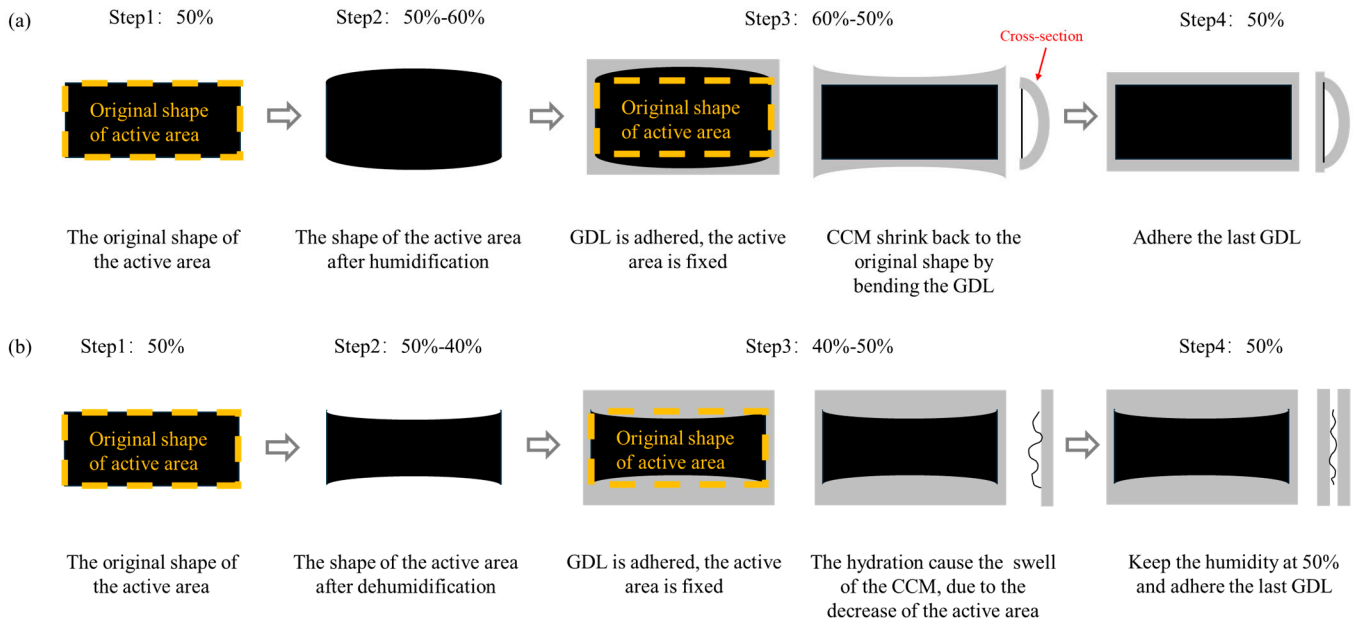


**Figure 16.** *Cont.*

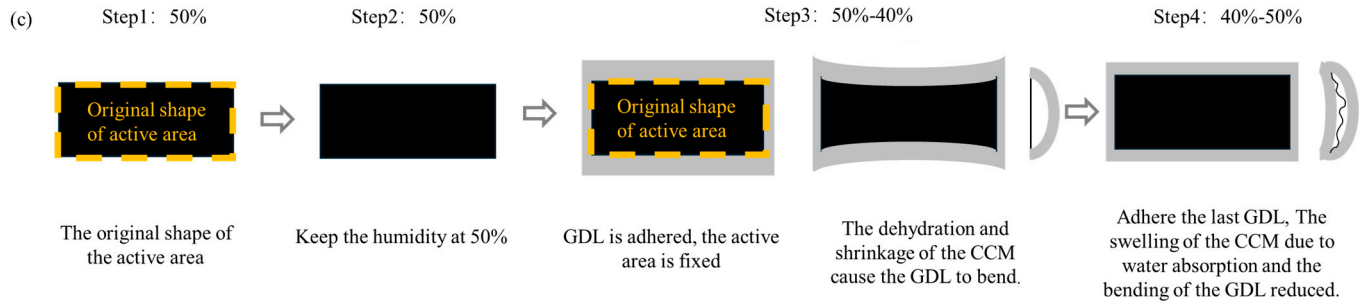


**Figure 16.** Schematic diagram explaining the deformation of the MEA after different humidity changes. (**a**) RH: 50-60-50-50 (%); (**b**) RH: 50-40-50-50 (%); and (**c**) RH: 50-50-40-50 (%).

## 6. Conclusions

This study measured the mechanical properties and hygroscopic expansion behavior of a PTFE-based catalyst-coated membrane (CCM) under different humidity levels and in various directions. A 3D numerical model was developed to simulate local climate control at different stages of the MEA production process chain. The simulation analyzed the effects of deviations in humidity on dimensional changes in the CCM, which subsequently resulted in stress and deformation of the MEA's subcomponents. The following conclusions were drawn from this study:

(1) The mechanical properties of the CCM, such as its Young's modulus and proportional limit stress, exhibit significant anisotropy and are influenced by humidity changes. The CCM experiments demonstrated isotropic hygroscopic swelling and shrinkage behavior. Any humidity changes during the MEA assembly process will result in in-plane stress and deformation.

(2) For the five-layer MEA, an excessive reduction in humidity causes great stress on the CCM and the GDL, leading to bending of the whole MEA assembly. Hence, the final product of the MEA's assembly should be stored in such an environment where excessively low humidity does not occur. On the contrary, humidity fluctuations above 50% can be quite well tolerated if the humidity can be restored before stacking.

(3) During the R2R process of MEA assembly, humidity control exactly at the step of the installation of the first GDL is more crucial. The humidity control after the attachment of the first GDL can be less strict, as resetting the humidity back to 50% afterward will not significantly increase the stress on the CCM.

(4) MEAs with only one GDL assembled should not be subjected to a humidity reduction process, as this will result in substantial bending deformation in the final assembled MEAs, which will not pass quality control for the stacking process and should be counted as scrap.

**Author Contributions:** Conceptualization, L.M. and J.F.; methodology, L.M.; software, Z.Y. and L.M.; validation, Z.Y.; formal analysis, L.M. and Z.Y.; investigation, L.M. and Z.Y.; resources, J.F.; data curation, L.M. and Z.Y.; writing—original draft preparation, Z.Y. and L.M.; writing—review and editing, L.M. and S.S.; visualization, Z.Y.; supervision, L.M.; project administration, L.M.; funding acquisition, L.M. and J.F. All authors have read and agreed to the published version of the manuscript.

**Funding:** This research was funded by the Baden-Württemberg Ministry for the Environment, Climate and Energy Sector under grant no. BWKWHF23107.

**Data Availability Statement:** The datasets presented in this article are not readily available because the data are part of an ongoing study. Requests to access the datasets should be directed to the corresponding author.

**Conflicts of Interest:** The authors declare no conflicts of interest.

## References

1. Basu, S. (Ed.) *Recent trends in Fuel Cell Science and Technology*; Springer: New York, NY, USA, 2007.

2. Wang, S.; Jiang, S.P. Prospects of fuel cell technologies. *Natl. Sci. Rev.* **2017**, *4*, 163–166. [CrossRef]
3. Thomas, C.E. Fuel cell and battery electric vehicles compared. *Int. J. Hydrog. Energy* **2009**, *34*, 6005–6020. [CrossRef]
4. Fultz, D.W.; Chuang, P.-Y.A. The Property and Performance Differences Between Catalyst Coated Membrane and Catalyst Coated Diffusion Media. *J. Fuel Cell Sci. Technol.* **2011**, *8*, 041010. [CrossRef]
5. Bock, A.; Klein, K.; Rakousky, C.; Barsch, H. Gas Diffusion Layer for Fuel Cells. US20220393184A1, 8 December 2022. Available online: https://patents.google.com/patent/US20220393184A1/en (accessed on 4 October 2024).
6. Tang, H.; Wang, S.; Jiang, S.P.; Pan, M. A comparative study of CCM and hot-pressed MEAs for PEM fuel cells. *J. Power Sources* **2007**, *170*, 140–144. [CrossRef]
7. Arcella, V.; Merlo, L.; Ghielmi, A. Proton exchange membranes for fuel cells. In *Advanced Membrane Science and Technology for Sustainable Energy and Environmental Applications*; Elsevier: Amsterdam, The Netherlands, 2011; pp. 465–495.
8. Kundu, S.; Simon, L.C.; Fowler, M.; Grot, S. Mechanical properties of Nafion$^{TM}$ electrolyte membranes under hydrated conditions. *Polymer* **2005**, *46*, 11707–11715. [CrossRef]
9. Tang, Y.; Karlsson, A.M.; Santare, M.H.; Gilbert, M.; Cleghorn, S.; Johnson, W.B. An experimental investigation of humidity and temperature effects on the mechanical properties of perfluorosulfonic acid membrane. *Mater. Sci. Eng. A* **2006**, *425*, 297–304. [CrossRef]
10. Shang, Z.; Hossain, M.d.M.; Wycisk, R.; Pintauro, P.N. Poly(phenylene sulfonic acid)-expanded polytetrafluoroethylene composite membrane for low relative humidity operation in hydrogen fuel cells. *J. Power Sources* **2022**, *535*, 231375. [CrossRef]
11. Kolde, J.A. Advanced Composite Polymer Electrolyte Fuel Cell Membranes. *ECS Proc. Vol.* **1995**, *1995–23*, 193–201. [CrossRef]
12. Tang, Y.; Kusoglu, A.; Karlsson, A.M.; Santare, M.H.; Cleghorn, S.; Johnson, W.B. Mechanical properties of a reinforced composite polymer electrolyte membrane and its simulated performance in PEM fuel cells. *J. Power Sources* **2008**, *175*, 817–825. [CrossRef]
13. Goulet, M.-A.; Khorasany, R.M.H.; De Torres, C.; Lauritzen, M.; Kjeang, E.; Wang, G.G.; Rajapakse, N. Mechanical properties of catalyst coated membranes for fuel cells. *J. Power Sources* **2013**, *234*, 38–47. [CrossRef]
14. Uchiyama, T.; Kato, M.; Ikogi, Y.; Yoshida, T. Mechanical Degradation Mechanism of Membrane Electrode Assemblies in Buckling Test Under Humidity Cycles. *J. Fuel Cell Sci. Technol.* **2012**, *9*, 061005. [CrossRef]
15. Sadeghi Alavijeh, A.; Bhattacharya, S.; Thomas, O.; Chuy, C.; Yang, Y.; Zhang, H.; Kjeang, E. Effect of hygral swelling and shrinkage on mechanical durability of fuel cell membranes. *J. Power Sources* **2019**, *427*, 207–214. [CrossRef]
16. Ramani, D.; Singh, Y.; White, R.T.; Wegener, M.; Orfino, F.P.; Dutta, M.; Kjeang, E. 4D in situ visualization of mechanical degradation evolution in reinforced fuel cell membranes. *Int. J. Hydrog. Energy* **2020**, *45*, 10089–10103. [CrossRef]
17. Park, J.; Kang, Z.; Bender, G.; Ulsh, M.; Mauger, S.A. Roll-to-roll production of catalyst coated membranes for low-temperature electrolyzers. *J. Power Sources* **2020**, *479*, 228819. [CrossRef]
18. Kang, H.; Lee, C. Effect of tension on conductivity of gravure printed Ag layer in roll-to-roll process. *Int. J. Precis. Eng. Manuf.* **2015**, *16*, 99–104. [CrossRef]
19. Lee, J.; Byeon, J.; Lee, C. Theories and Control Technologies for Web Handling in the Roll-to-Roll Manufacturing Process. *Int. J. Precis. Eng. Manuf.-Green Technol.* **2020**, *7*, 525–544. [CrossRef]
20. Grenfell, K.P. Tension Control Paper-Making and Converting Machinery. *IEEE Trans. Appl. Ind.* **1964**, *83*, 234–240. [CrossRef]
21. Finn, M.; Martens, C.J.; Zaretski, A.V.; Roth, B.; Søndergaard, R.R.; Krebs, F.C.; Lipomi, D.J. Mechanical stability of roll-to-roll printed solar cells under cyclic bending and torsion. *Sol. Energy Mater. Sol. Cells* **2018**, *174*, 7–15. [CrossRef]
22. Zhang, X.A.; Jiang, Y.; Venkatesh, R.B.; Raney, J.R.; Stebe, K.J.; Yang, S.; Lee, D. Scalable Manufacturing of Bending-Induced Surface Wrinkles. *ACS Appl. Mater. Interfaces* **2020**, *12*, 7658–7664. [CrossRef]
23. Kusoglu, A.; Karlsson, A.M.; Santare, M.H.; Cleghorn, S.; Johnson, W.B. Mechanical response of fuel cell membranes subjected to a hygro-thermal cycle. *J. Power Sources* **2006**, *161*, 987–996. [CrossRef]
24. Uchiyama, T.; Kumei, H.; Yoshida, T. Catalyst layer cracks by buckling deformation of membrane electrode assemblies under humidity cycles and mitigation methods. *J. Power Sources* **2013**, *238*, 403–412. [CrossRef]
25. *DIN EN ISO 527-3*; Plastics—Determination of Tensile Properties—Part 3: Test Conditions for Films and Sheets. DIN Deutsches Institut für Normung e. V.: Berlin, Germany, 2019.
26. Valentine, S.; James, R.L.; Healy, J.P.; Lakshmanan, B. Manufacture of Unitized Electrode Assembly for PEM Fuel Cells. US7569082B2, 4 August 2009. Available online: https://patents.google.com/patent/US7569082B2/en?oq=US+7,569,082+B2 (accessed on 28 June 2024).
27. Ouerghemmi, M.; Carral, C.; Mele, P. Determination of the Orthotropic Mechanical Elastic Properties of Gas Diffusion Layers for PEMFCs. *J. Electrochem. Soc.* **2023**, *170*, 104508. [CrossRef]
28. Jamshidi, M.; Shokrieh, M.M. On the Schapery nonlinear viscoelastic model: A review. *Eur. J. Mech.-A/Solids* **2024**, *108*, 105403. [CrossRef]
29. Chailleux, E.; Davies, P. Modelling the Non-Linear Viscoelastic and Viscoplastic Behaviour of Aramid Fibre Yarns. *Mech. Time-Depend. Mater.* **2003**, *7*, 291–303. [CrossRef]
30. *ASTM D882*; Standard Test Method for Tensile Properties of Thin Plastic Sheeting. ASTM International: West Conshohocken, PA, USA, 2018.
31. Woo, H.J.; Lee, K.S. Membrane Electrode Assembly. US10886550B2, 5 January 2021. Available online: https://patents.google.com/patent/US10886550B2/en?q=(subgasket)&q=(gas+diffusion+layer)&assignee=hyundai (accessed on 5 October 2024).

32. Iverson, E.J.; Pierpont, D.M.; Yandrasits, M.A.; Hamrock, S.J.; Obradovich, S.J.; Peterson, D.G. Fuel Cell Subassemblies Incorporating Subgasketed Thrifted Membranes. US20110151350A1, 23 June 2011. Available online: https://patents.google.com/patent/US20110151350A1/en?oq=US20110151350A1 (accessed on 1 March 2024).
33. Ringk, A.; Ringel, A. Membrane-Electrode Unit for an Electrochemical Cell, and Method for Manufacturing a Membrane-Electrode Unit. US20230378506A1, 23 November 2023. Available online: https://patents.google.com/patent/US20230378506A1/en?oq=US20230378506A1 (accessed on 7 February 2024).
34. Joye, O. Assemblage Membrane-Électrode de Pile à Combustible, Procédé de Fabrication d'un tel Assemblage et Pile à Combustible Comprenant au Moins un tel Assemblage. FR3132394B3, 22 March 2024. Available online: https://patents.google.com/patent/FR3132394B3/en?oq=FR3132394B3 (accessed on 5 October 2024).
35. Chen, J.; Liu, H.; Huang, Y.; Yin, Z. High-rate roll-to-roll stack and lamination of multilayer structured membrane electrode assembly. *J. Manuf. Process.* **2016**, *23*, 175–182. [CrossRef]
36. Randová, A.; Bartovská, L.; Hovorka, Š.; Kačírková, M.; Vychodilová, H.; Sedláková, Z.; Šťastná, L.Č.; Brožová, L.; Žitka, J.; Sysel, P.; et al. Sorption of enantiomers and alcohols into Nafion® and the role of air humidity in the experimental data evaluation. *Sep. Purif. Technol.* **2015**, *144*, 232–239. [CrossRef]